

# Demixing is a default process for biological condensates formed via phase separation

Shihan Zhu<sup>1,3†</sup>, Zeyu Shen<sup>1,3†</sup>, Xiandeng Wu<sup>1</sup>, Wenyan Han<sup>2</sup>, Bowen Jia<sup>1</sup>, Wei Lu<sup>2</sup>, Mingjie Zhang<sup>3\*</sup>

Excitatory and inhibitory synapses do not overlap even when formed on one submicron-sized dendritic protrusion. How excitatory and inhibitory postsynaptic cytomatrices or densities (e/iPSDs) are segregated is not understood. Broadly, why membraneless organelles are naturally segregated in cellular subcompartments is unclear. Using biochemical reconstitutions in vitro and in cells, we demonstrate that ePSDs and iPSDs spontaneously segregate into distinct condensed molecular assemblies through phase separation. Tagging iPSD scaffold gephyrin with a PSD-95 intrabody (dissociation constant ~4 nM) leads to mistargeting of gephyrin to ePSD condensates. Unexpectedly, formation of iPSD condensates forces the intrabody-tagged gephyrin out of ePSD condensates. Thus, instead of diffusion-governed spontaneous mixing, demixing is a default process for biomolecules in condensates. Phase separation can generate biomolecular compartmentalization specificities that cannot occur in dilute solutions.

**S**egregation of excitatory and inhibitory signals into distinct subcompartments in each neuron provides a foundation for excitatory and inhibitory balance of neuronal circuits (1, 2), a process important for the brain to function properly. An excitatory synapse contains a layer of electron-dense thickening and cytomatrix that is ~50 nm thick and several hundred nanometers wide and is known as postsynaptic density (PSD) (3–5). Electron-dense thickenings of inhibitory synapses also exist but are much thinner (~15 nm) (3, 6, 7). The vast majority of inhibitory synapses are located on dendritic shafts. A sizable proportion of inhibitory synapses are co-innervated onto excitatory spine protrusions (8–12). The anatomic structures of dually innervated spines—particularly their postsynaptic compartments—are intriguing. Electron microscopic studies have revealed that the excitatory and inhibitory PSDs (ePSDs and iPSDs) in each dually innervated spine form well-separated, electron-dense subcompartments within a submicron-sized spine protrusion (9, 13, 14). It is well established that ePSDs and iPSDs are formed by distinct sets of proteins capable of concentrating  $\alpha$ -amino-3-hydroxy-5-methyl-4-isoxazolepropionic acid (AMPA) receptors or *N*-methyl-D-aspartate (NMDA) receptors (AMPA or NMDARs) and  $\gamma$ -aminobutyric acid (GABA) or glycine receptors (GABA<sub>A</sub>Rs or GlyRs), respectively, into dense clusters to conduct opposite electric currents (15–19). The dense ePSD and iPSD molecular

assemblies do not disperse and do not mix even though they share a dilute spine cytoplasm (Fig. 1A).

Recent studies have demonstrated that specific and multivalent interactions of synaptic proteins lead to autonomous formation of highly condensed PSD assemblies through phase separation for both ePSDs and iPSDs (20–23). Phase separation provides a distinctive molecular mechanism for PSD condensate formation that cannot be explained by conventional protein-protein interactions in dilute solutions (fig. S1). However, the molecular basis governing spatial segregation of ePSD and iPSD condensates is unclear. The segregation between ePSDs and iPSDs also represents a prototypical example for numerous cellular membraneless organelles that coexist and function in various cellular subcompartments (24–29). A pressing question in phase separation research is how numerous membraneless organelles can segregate from each other in cells, considering that these organelles do not contain physical barriers.

Using a biochemical reconstitution approach in vitro and in cells, we discovered that the ePSD and iPSD condensates formed through phase separation were intrinsically segregated. We found that phase separation-mediated formation of biological condensates generated molecular interaction and compartmentalization specificities that did not occur in dilute solutions. Our study suggests that demixing is a default process for biological condensates formed through phase separation.

## ePSD and iPSD components segregate into distinct condensates through phase separation

We previously showed that mixing four major ePSD scaffold proteins (PSD-95, GKAP, Shank3, and Homer3, each being a multidomain scaffold protein capable of specifically interacting

with other proteins forming a large, peripheral network; Fig. 1A and table S1) leads to the formation of ePSD condensates capable of enriching Ras guanosine triphosphatase (GTPase) SynGAP and clustering Stargazin (an auxiliary subunit of AMPARs) (21, 22). We also demonstrated that mixing the key iPSD scaffold gephyrin (the full-length protein GPHN-FL or its E-domain GPHN-E) with dimerized GlyR (GlyR- $\beta$ LD) or GABA<sub>A</sub>R cytoplasmic loop (GABA<sub>A</sub>R- $\alpha$ 3LD) leads to the formation of iPSD condensates (Fig. 1A) (20). In this study, we asked what might happen when we mixed five purified ePSD proteins (PSD-95, GKAP, Shank3, Homer3, and SynGAP $\alpha$ 1; referred to as 5xePSD) with two iPSD proteins (GPHN-E and GlyR- $\beta$ LD; referred to as 2xiPSD) in a test tube (Fig. 1A). When the seven proteins were mixed, the ePSD and iPSD components formed two distinct condensates (Fig. 1B and movie S1; quantified in fig. S2A).

Addition of the cytoplasmic tail of Stargazin (Stg\_CT) into the seven e/iPSD mixture led to its specific enrichment into the ePSD condensates (Fig. 1C; quantified in fig. S2B). The PDZ binding motif of Stg\_CT specifically binds to PSD-95 PDZ2, and this binding is critical for enriching Stg\_CT into 5xePSD condensates (21). Consistently, removal of the last four residues from Stg\_CT (“Stg\_d4”) substantially reduced its enrichment in 5xePSD condensates. Stg\_d4 instead became enriched into the iPSD condensates (Fig. 1D and fig. S2C), presumably because of weak electrostatic interaction between positively charged Stg\_d4 and negatively charged GPHN-E. This finding suggests a critical role of the specific interaction between Stg\_CT and PSD-95 in targeting Stg\_CT into the proper PSD subcompartment and in suppressing nonspecific interaction-mediated compartmentalization. Similarly, we specifically disrupted the interaction between GPHN and GlyR- $\beta$ LD by replacing Phe420 and Ile422 of GlyR- $\beta$ LD with Ala. The mutant GlyR- $\beta$ LD (“GlyR- $\beta$ LD\_FAIA”) no longer formed condensates with GPHN (20). Both the GlyR- $\beta$ LD mutant and GPHN-E became enriched into ePSD condensates (fig. S3), again presumably because of weak and nonspecific interactions between the two iPSD proteins and ePSD proteins.

The G375D mutant of GPHN, identified in patients with Dravet-like syndrome (30), does not alter its binding to GlyR- $\beta$ LD, but the mutant could no longer phase separate with GlyR- $\beta$ LD [Fig. 1E, top row; as reported in (20)]. Mixing the GPHN-E mutant and GlyR- $\beta$ LD with 5xePSD again did not cause the separation of the iPSD proteins from ePSD condensates (Fig. 1E, top row). We next substituted tetrameric Homer3 with monomeric Homer1a in the 5xePSD system. This change substantially weakened phase separation of ePSDs [Fig. 1E, bottom row; as reported in

<sup>1</sup>Division of Life Science, Hong Kong University of Science and Technology, Hong Kong, China. <sup>2</sup>Synapse and Neural Circuit Research Section, National Institute of Neurological Disorders and Stroke, National Institutes of Health, Bethesda, MD 20824, USA. <sup>3</sup>School of Life Sciences, Southern University of Science and Technology, Shenzhen 518055, China.

\*Corresponding author: zhangmj@sustech.edu.cn

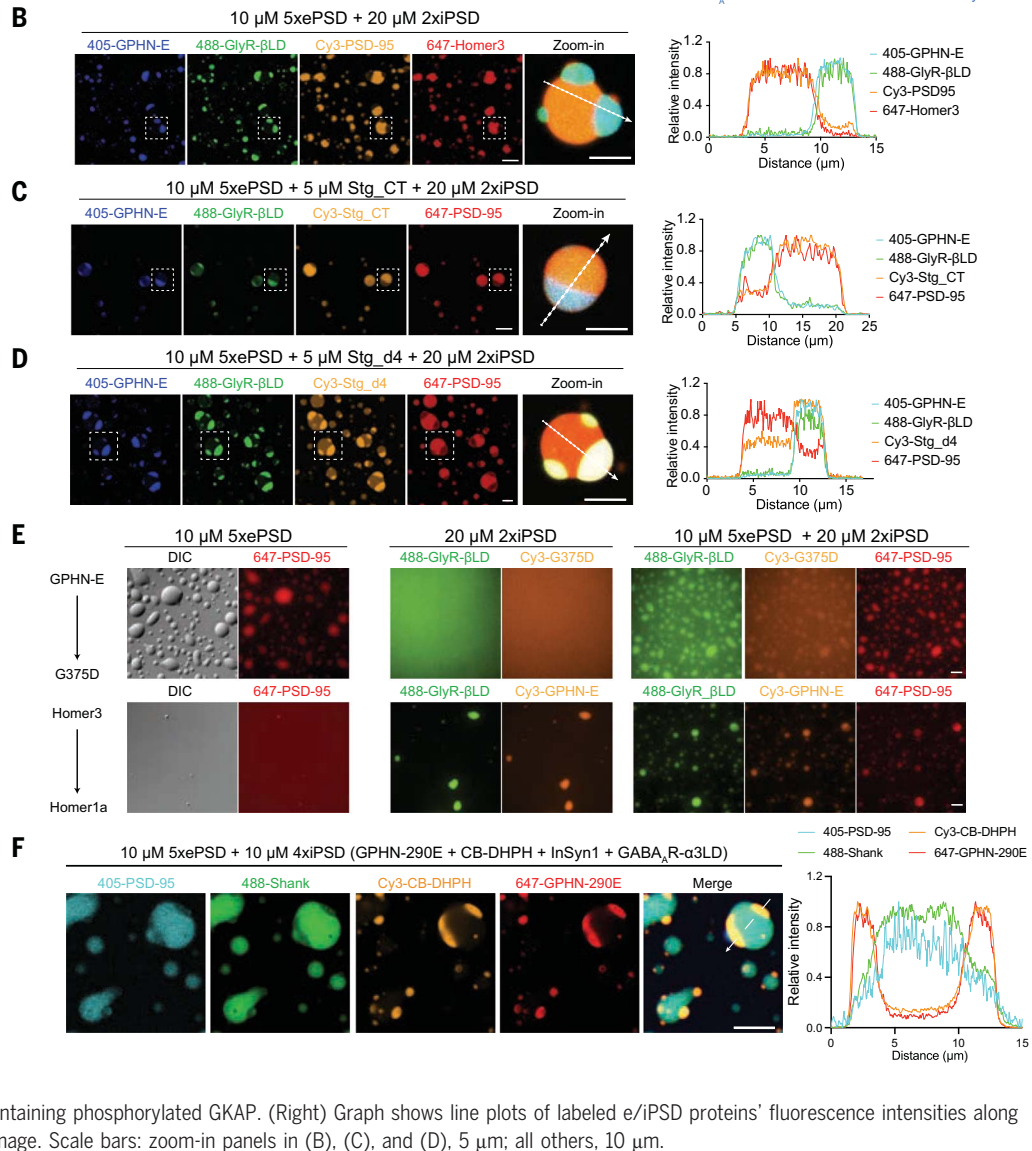
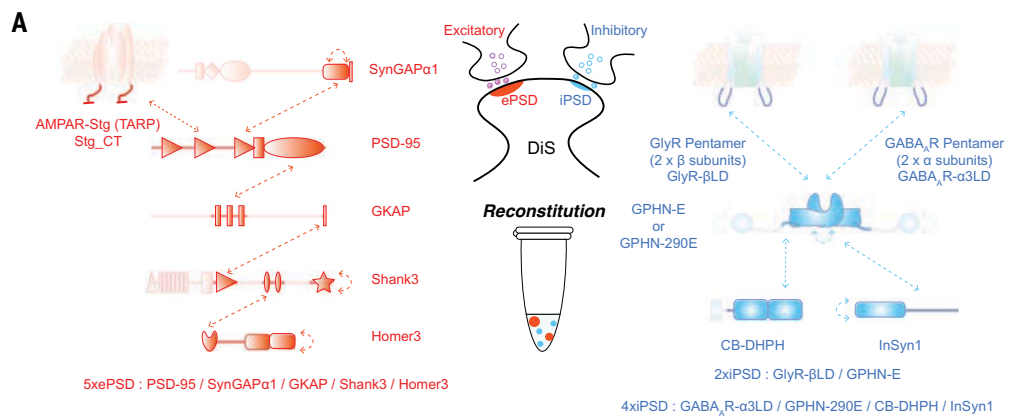
†These authors contributed equally to this work.



### Fig. 1. Phase separation-mediated segregation of ePSD and iPSD condensates.

#### (A) A schematic showing PSD proteins used in the reconstitution assays.

Recombinant proteins for the 5xePSD system (left) are the same as those described earlier (22). The iPSD proteins for the 2xiPSD system (right) were described previously (20) and with other iPSD scaffold proteins as described in this study (also see table S1). Dashed lines indicate the interaction between domains. The shaded parts were removed from the recombinant proteins used in our reconstitution assays. (Middle, top panel) Schematic diagram of a dually innervated spine (DiS).



(B) Fluorescence images showing the segregation of 5xePSD condensates from 2xiPSD condensates. For the 5xePSD system, only PSD-95 and Homer3 were fluorescence labeled and the other three proteins were not labeled and thus invisible. The final concentration of each protein in the mixture is indicated above the images (e.g., 10  $\mu$ M for each ePSD protein and 20  $\mu$ M for each iPSD protein); this scheme is used throughout the figures. In (B), (C), and (D) the region indicated with the dashed boxes is selected for zoom-in and for detailed line-scanning analysis (right panel).

(C) Mixing of Stg\_CT with the ePSD and iPSD condensates led to specific recruitment of Stg\_CT into ePSD condensates. (D) In contrast to Stg\_CT, mixing Stg\_CT without PBM ("Stg\_d4") led to mistargeting of Stg\_d4 into the iPSD condensates.

(E) Phase separation-defective proteins cannot support segregation of e/iPSD condensates. Panels indicate phase separation of the 5xePSD only (left), 2xiPSD only (middle), and the mixtures of 5xePSD and 2xiPSD components (right) under each assay condition. (Top row) WT GPHN-E was replaced by the G375D mutant (where glycine at position 375 was replaced with aspartic acid). (Bottom row) Tetrameric Homer3 was substituted by monomeric Homer1a.

(F) (Left) Fluorescence images showing mixtures of 4xiPSD (GPHN-290E, CB-DHPH, InSyn1, and GABA<sub>A</sub>R- $\alpha$ 3LD) condensates with 5xePSD condensates containing phosphorylated GKAP. (Right) Graph shows line plots of labeled e/iPSD proteins' fluorescence intensities along the dashed line in adjacent left (Merge) image. Scale bars: zoom-in panels in (B), (C), and (D), 5  $\mu$ m; all others, 10  $\mu$ m.

(22)]. Upon mixing the Homer1a-containing 5xePSD protein mixture with GlyR- $\beta$ LD and GPHN-E, only iPSD condensates were formed, and no segregation of iPSD with ePSD components was observed (Fig. 1E, bottom row). These results revealed that formation of the ePSD

and the iPSD condensates does not depend on each other. However, the segregation of e/iPSD components strictly depends on the phase separation of both PSD condensates.

Homer1a, the product of the immediate early gene *Homer1a*, is rapidly induced by neuronal

activities (31). The rise of Homer1a concentration leads to down regulation of ePSD formation in vivo and in vitro (22, 31, 32). We found that addition of Homer1a to the ePSD/iPSD condensate mixtures effectively dispersed ePSD condensates only (fig. S4), indicating that

(22)]. Upon mixing the Homer1a-containing 5xePSD protein mixture with GlyR- $\beta$ LD and GPHN-E, only iPSD condensates were formed, and no segregation of iPSD with ePSD components was observed (Fig. 1E, bottom row). These results revealed that formation of the ePSD

and the iPSD condensates does not depend on each other. However, the segregation of e/iPSD components strictly depends on the phase separation of both PSD condensates.

Homer1a, the product of the immediate early gene *Homer1a*, is rapidly induced by neuronal

activities (31). The rise of Homer1a concentration leads to down regulation of ePSD formation in vivo and in vitro (22, 31, 32). We found that addition of Homer1a to the ePSD/iPSD condensate mixtures effectively dispersed ePSD condensates only (fig. S4), indicating that

segregated ePSD and iPSD condensates can be independently regulated.

GABA<sub>A</sub>Rs are more abundant in the central nervous system than GlyRs (33). We found that the GABA<sub>A</sub>R-containing iPSD condensates were also segregated from ePSD condensates (fig. S5, A and B). Collybistin (CB) and InSyn1 are additional iPSD scaffold proteins that can directly bind to GPHN (34–36). We elaborated our reconstitution system by mixing purified InSyn1 and the DH-PH tandem of CB (CB-DHPPH) with GABA<sub>A</sub>R- $\alpha$ 3LD and GPHN-290E which contains an N-terminal extension responsible for CB interaction (Fig. 1A and table S1) (37). The four iPSD proteins together formed 4xiPSD condensates (fig. S5, C and D). When the 4xiPSD mixture was mixed with the 5xePSD mixture, the formed iPSD condensates were also segregated from the ePSD condensates (Fig. 1F; quantified in fig. S2D).

### e/iPSD scaffold proteins induce segregation of membrane-bound receptors

We asked whether segregation of the ePSD and iPSD condensates could occur on the membrane surface of giant unilamellar vesicles (GUVs) tethered with GlyR- $\beta$ LD and/or Stg\_CT (Fig. 2A). Without scaffold proteins, His<sub>6</sub>-GlyR- $\beta$ LD or His<sub>6</sub>-Stg\_CT was homogeneously distributed on the GUV surfaces (Fig. 2B). Addition of GPHN-E to the GlyR- $\beta$ LD-tethered GUV solution led to co-clustering of GPHN-E and GlyR- $\beta$ LD on the membrane surface, and these iPSD clusters with irregular shapes were formed through spinodal decomposition-mediated phase separation (Fig. 2C, fig. S6A, and movie S2; quantified in fig. S7A). Similarly, addition of ePSD scaffold proteins to Stg\_CT-tethered GUV solutions led to co-phase separation of Stg\_CT with the scaffold proteins (Fig. 2D and fig. S6B; quantified in fig. S7B). The iPSD or ePSD condensate formation on the GUV surfaces was specific for the protein components, as Cy5-PE signal remained homogeneous (Fig. 2, C and D).

For reconstituting e/iPSDs together on the membrane surface, both His<sub>6</sub>-GlyR- $\beta$ LD and His<sub>6</sub>-Stg\_CT were coated on the GUV surfaces with a comparable density (fig. S8A). When His<sub>6</sub>-GlyR- $\beta$ LD and His<sub>6</sub>-Stg\_CT were simultaneously tethered to GUVs, the two proteins were homogeneously distributed (Fig. 2, E and F, top rows; quantified in fig. S7C). GlyR- $\beta$ LD and Stg\_CT formed discrete condensates on the membrane surface of GUVs upon addition of ePSD scaffold proteins and GPHN-E (Fig. 2, E and F, bottom rows, and movie S3). When only GPHN-E was added into the GUVs coated with Stg\_CT and GlyR- $\beta$ LD, only iPSD condensates were formed and Stg\_CT was partially enriched into iPSD condensates (fig. S8B). Similarly, addition of ePSD scaffold proteins only induced Stg\_CT clustering on the GUV surfaces; GlyR- $\beta$ LD did not form segregated clusters but instead was enriched into ePSD

condensates (fig. S8C). Besides the membrane-tethered receptor tails, probing with scaffold proteins [PSD-95 and Homer3 for ePSD (Fig. 2G and fig. S8D); GPHN-E or GPHN\_FL for iPSD (Fig. 2G)] also showed that ePSD and iPSD condensates formed segregated clusters on the GUV surfaces (Fig. 2H; quantified in fig. S6D; also see fig. S5E to G for membrane-tethered GABA<sub>A</sub>R- $\alpha$ 3LD). Lastly, ePSD and iPSD condensates were also segregated on the surface of GUVs containing 1% phosphatidylinositol 4,5-bisphosphate and 1% phosphatidylinositol (3,4,5)-trisphosphate (fig. S9).

### ePSD and iPSD form discrete condensates but share a common dilute phase

Under conventional wide-field imaging, e/iPSD condensates appeared to cover the entire surface of the vesicle membrane, as if there were no dilute phase separating ePSD and iPSD condensates (Fig. 2I, top panel, and Fig. 3A). Structured illumination microscopy (SIM) images of PSD-95 and GPHN-E in the PSD condensates showed that ePSD and iPSD condensates on GUV surfaces were clearly separated and that the two types of PSDs shared a common dilute phase (Fig. 2I, bottom panel). The reconstructed super-resolution images acquired with the highly inclined and laminated optical sheet (HILO) illumination mode also showed that ePSD (marked by Alexa 555-Stg\_CT) and iPSD (marked by Alexa 647-GlyR- $\beta$ LD) condensates were clearly separated by membrane regions with low protein signals (Fig. 3B).

We next asked whether our reconstituted PSD condensates could trap membrane-bound receptors in the condensed phases on GUV surfaces analogous to what was observed in vivo by single-molecule tracking (38, 39). Without PSD scaffolds added, both Stg\_CT and GlyR- $\beta$ LD could freely diffuse on the membrane surface (Fig. 3C). Formation of ePSD and iPSD condensates enriched the two proteins into condensates and substantially slowed down the diffusions of both Stg\_CT and GlyR- $\beta$ LD (Fig. 3, D to F), indicating trapping of the receptors in the respective PSD condensates. Single-molecule tracking experiments further showed that both Stg\_CT and GlyR- $\beta$ LD switched between mobile states and confined states within each type of condensate (Fig. 3D and fig. S10), indicating the formation of percolated networks for both ePSD and iPSD condensates (40). The diffusion coefficients of Stg\_CT and GlyR- $\beta$ LD in the condensates on GUV surface (Fig. 3F and fig. S10C) are also at a similar range to those measured for AMPARs and GlyRs in synapses of living neurons (41–45).

### ePSD and iPSD condensates reconstituted in cells are also segregated

We next reconstituted ePSDs and iPSDs in HeLa cells. An advantage of using HeLa cells is that the ePSD and iPSD proteins are not

endogenously expressed there. We used two plasmids to express four ePSD scaffold proteins (PSD-95, GKAP, Shank3, and Homer3) and two iPSD proteins (GlyR- $\beta$ LD and GPHN-FL) (Fig. 3G). The concentrations of the expressed proteins in puncta in HeLa cells were within the concentration ranges of these proteins found in synapses (fig. S11D) (18, 46, 47). When the two plasmids were co-transfected, PSD-95 and GlyR- $\beta$ LD were distributed to two discrete types of droplet-like puncta in the cytosol (Fig. 3, H and I), indicating the formation of segregated ePSD and iPSD assemblies. In all cells imaged, we could observe fusions between GlyR- $\beta$ LD droplets or between PSD-95 droplets (Fig. 3J). No fusion events between GlyR- $\beta$ LD droplets and PSD-95 droplets were observed. Thus, ePSD and iPSD condensates formed in living cells are also segregated.

### GPHN tagged with a PSD-95 binding intrabody is enriched into ePSD condensates as a client protein

We next investigated the molecular mechanism governing the segregation of ePSD condensates from iPSD condensates. PSD-95.FingR, a small PSD-95 Src homology 3-guanylate kinase-like domain tandem (SH3-GK) recognizing intrabody (abbreviated as “95FR”) (48), has been widely used as an endogenous PSD-95 marker and for targeting exogenous proteins to ePSD in neurons (14, 48, 49). We characterized that 95FR bound to the PSD-95 PDZ-SH3-GK (PSG) tandem with a high affinity [dissociation constant ( $K_d$ ) ~4 nM; Fig. 4A]. We fused 95FR to the C terminus of GPHN-290E (“GPHN-290E-95FR”; Fig. 4B). GPHN-290E-95FR formed stable and stoichiometric complex with PSD-95\_PSG (Fig. 4C).

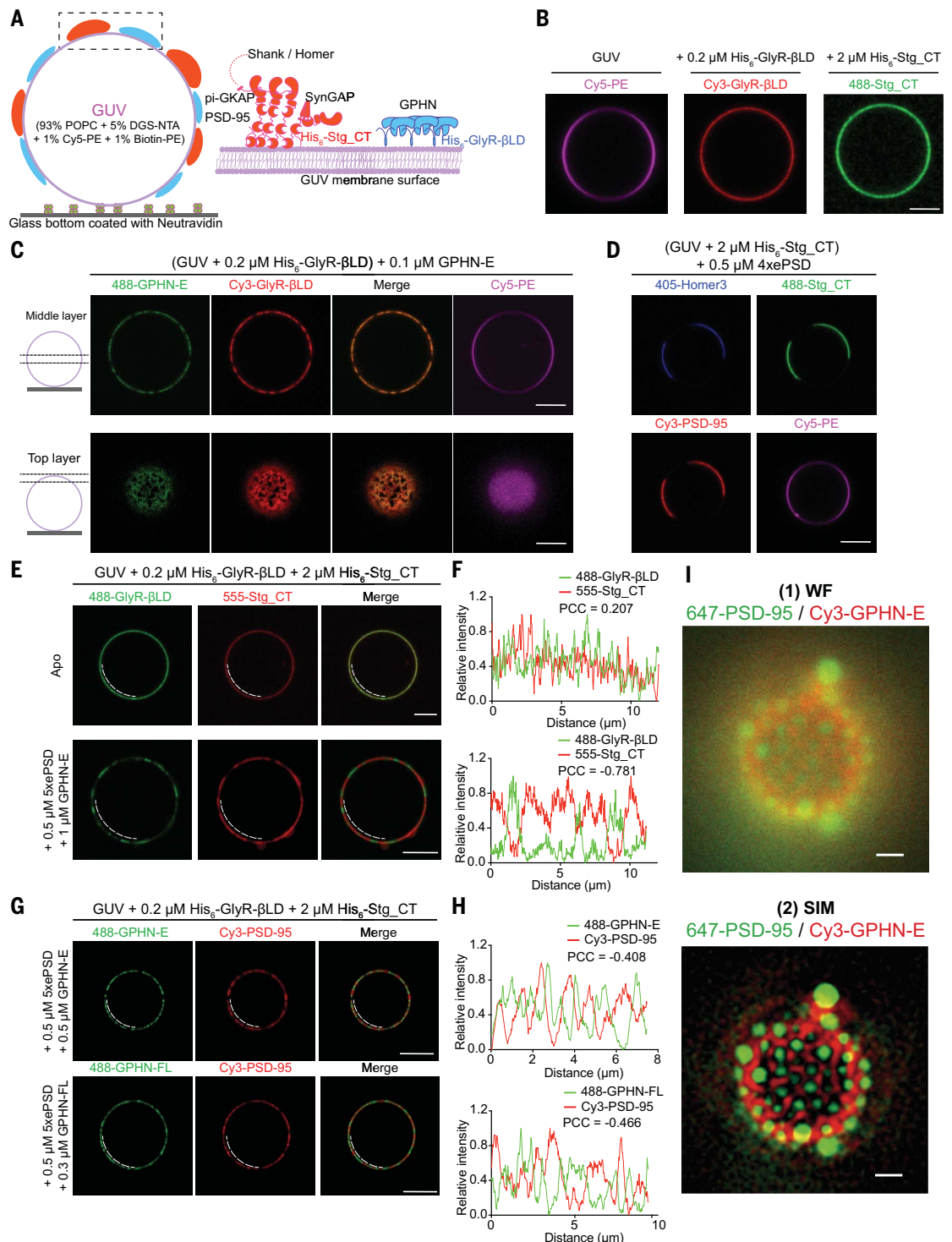
As expected, PSD-95 alone was only marginally enriched in the 4xiPSD condensates (Fig. 4D, left panels). GPHN-290E alone was not enriched in the 5xePSD condensates (Fig. 4E, left panels). By contrast, PSD-95 was recruited into the 4xiPSD condensates containing GPHN-290E-95FR (Fig. 4D, right panels), likely owing to the forced binding of PSD-95 with GPHN-290E-95FR. Similarly, GPHN-290E-95FR alone could be effectively targeted into 5xePSD condensates through the binding of GPHN-290E-95FR to PSD-95 (i.e., GPHN-290E-95FR is a client of the ePSD condensates) (Fig. 4E).

### Formation of iPSD condensates forces GPHN-290E-95FR to dissociate from ePSD condensates

We induced iPSD formation by mixing CB and GABA<sub>A</sub>R- $\alpha$ 3LD—or CB, InSyn1, and GABA<sub>A</sub>R- $\alpha$ 3LD—with GPHN-290E-95FR and combined these iPSD mixtures with the 5xePSD condensates (Fig. 4, F to I). We observed that GPHN-290E-95FR was excluded from the ePSD condensates and became enriched in the iPSD condensates (Fig. 4, F to I; quantified in fig. S12).

## Fig. 2. PSD scaffold proteins form distinct condensates with respective receptors on GUV membrane surfaces.

**(A)** Schematic diagram showing reconstitutions of ePSD and iPSD on the GUV surface. (Left) GUVs were immobilized on the glass surface through binding to coated neutravidin. ePSD (red ovals) and iPSD (blue ovals) condensates were formed on the GUV membrane through binding to membrane-tethered His<sub>6</sub>-Stg\_CT or His<sub>6</sub>-GlyR-βLD (right). In the GUV-based reconstitution assays, unbound His<sub>6</sub>-tagged receptors were washed away through serial dilution before addition of PSD scaffold proteins. Because of the much lower protein concentrations used in the reconstitutions, fluorescence labeling for each protein was raised to 5% to increase the sensitivity of imaging experiments. **(B)** Membrane-tethered GlyR-βLD or Stg\_CT, in the absence of PSD scaffold proteins, was homogeneously distributed on the GUV membrane surface. (Left) Cy5-PE was used to mark the GUV membranes. (Middle) Only His<sub>6</sub>-GlyR-βLD was tethered to the GUV. (Right) Only His<sub>6</sub>-Stg\_CT was tethered to the GUV. **(C)** Fluorescence images showing formation of the GPHN-E/GlyR-βLD condensates on the GUV surface. GPHN-E at 0.1 μM was added to the solution containing GUVs tethered with 0.2 μM His<sub>6</sub>-GlyR-βLD. (Top row) Images taken at the middle optical section along the z direction of the vesicle. (Bottom row) Images taken at the top layer of the same vesicle. **(D)** Fluorescence images showing the formation of ePSD condensates on the GUV surface. Four ePSD scaffold proteins (PSD-95, pi-GKAP, Shank3, and Homer3, each at 0.5 μM) were added into solution of GUVs that were tethered with His<sub>6</sub>-Stg\_CT. **(E)** Distributions of membrane-tethered GlyR-βLD and Stg\_CT without (top row) or with (bottom row) addition of 0.5 μM 5xePSD and 1 μM GPHN-E. **(F)** Line plots of GlyR-βLD and Stg\_CT fluorescence signal intensities along the dashed line in (E). Top graph shows results without PSD scaffold proteins; bottom graph shows results with PSD scaffold proteins. Pearson correlation coefficient (PCC) was calculated on the basis of the distribution shown in the line plots. **(G)** Distributions



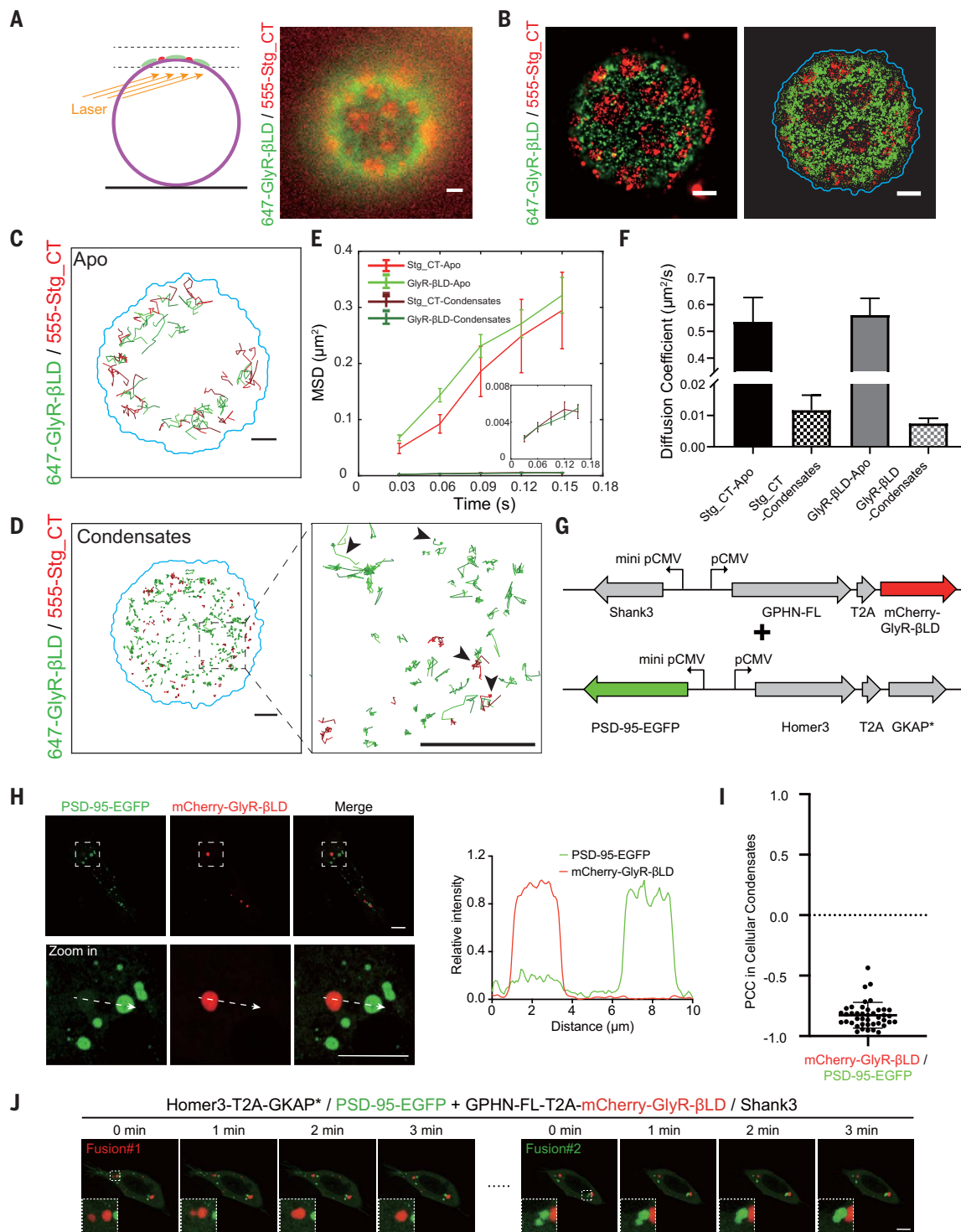


**Fig. 3. ePSD and iPSD condensates formed on membrane surfaces share a common dilute phase in vitro and in heterologous cells.** (A) Schematic diagram showing super-resolution imaging and single-molecule tracking of e/iPSD proteins on the GUV surfaces. For all super-resolution imaging, GUVs were coated with 2  $\mu\text{M}$  Alexa 555-Stg\_CT and 0.2  $\mu\text{M}$  Alexa 647-GlyR- $\beta\text{LD}$ . Condensates were induced by adding 0.5  $\mu\text{M}$  5xePSD and 0.3  $\mu\text{M}$  GPHN-FL. (Left) HILO mode illumination was used to image the very top section of the immobilized GUV. (Right) A representative wide-field fluorescence image of Stg\_CT and GlyR- $\beta\text{LD}$  from ePSD and iPSD condensates formed on the surface of a GUV. (B) Super-resolution image of the GUV shown in (A) rendered with

Thunder STORM (left) and molecular localizations (right) of Stg\_CT and GlyR- $\beta\text{LD}$  from ePSD and iPSD condensates, respectively. Light-blue line denotes the boundary between all molecular localizations on GUV membrane and the dilute solution in the system. (C) and (D) Representative trajectories of Stg\_CT (red) and GlyR- $\beta\text{LD}$  (green) tethered onto the surface of GUV with or without addition of PSD scaffold proteins. In (C), only Stg\_CT and GlyR- $\beta\text{LD}$  were tethered to the GUVs (apo form). In (D), 5xePSD and GPHN-FL were added to induce condensates formation, and trajectories were extracted from the same GUV as shown in (A) and (B). Zoom-in of a small section in D (right) is to show typical motion switches of both Stg\_CT and GlyR- $\beta\text{LD}$  confined states

and mobile states. **(E)** Plots of mean square displacement (MSD) as a function of time for Stg\_CT and GlyR- $\beta$ LD trajectories on GUV surfaces without or with addition of PSD scaffold proteins. The scale of the y axis for Stg\_CT and GlyR- $\beta$ LD in the PSD condensates is enlarged and shown as an insert. Error bar is defined as SD. **(F)** Average diffusion coefficients of Stg\_CT and GlyR- $\beta$ LD on GUV surfaces. Data were derived from three independent batches of experiments. Error bar is defined as SD. **(G)** Protein constructs used for expressions of ePSD and iPSD components in HeLa cells. Except for GKAP, the rest of ePSD and iPSD components expressed in cells are the same as the recombinant proteins used in Fig. 1. A designed DLS peptide sequence mimicking the phosphorylated GK domain binding repeat (56) was used to replace the GK domain binding repeats of GKAP [the resulting modified GKAP is defined as "GKAP\*" (57)]. "T2A" stands for the autocleavable sequence linking two

genes connected in tandem. **(H)** (Left) Representative fluorescence images of cells showing segregated puncta enriched either with PSD-95 or GlyR- $\beta$ LD. In essentially every transfected cell, ePSD puncta and iPSD puncta were segregated, thus no quantification is needed. (Right) Graph shows line plots of PSD-95 and GlyR- $\beta$ LD fluorescence signals along the dashed lines shown at left. **(I)** Quantification of e/iPSD puncta segregation measured by plotting PCC values of PSD-95 versus GlyR- $\beta$ LD from cells transfected with plasmids shown in (H). Data were collected from three independent batches.  $n = 43$  cells. Error bars indicate  $\pm$  SD. **(J)** Time-lapse images of one representative HeLa cell with e/iPSD components coexpressed to show fusions of iPSD droplets and ePSD droplets. (Left) Fusion between two iPSD droplets marked by mCherry-GlyR- $\beta$ LD. (Right) Fusion between two ePSD droplets marked by PSD-95-EGFP. Scale bars: 1  $\mu$ m for (A) to (D); 10  $\mu$ m for (H) and (J).

CB did not have detectable impact on the binding between GPHN-290E-95FR and PSD-95 (fig. S13), ruling out a possibility of a direct competition between CB and 95FR in binding to PSD-95. The results in Fig. 4 reveal that formation of iPSD and ePSD condensates can force apart a strong interaction ( $K_d \sim 4$  nM) between GPHN-290E-95FR and PSD-95, allowing formation of segregated ePSD and iPSD condensates in vitro. The results also indicate that phase separation-mediated formation of biological condensates can fundamentally alter molecular interactions and compartmentalization that occur in dilute solutions.

PSD-95 appeared to be evenly distributed in both ePSD and iPSD condensates in the above GPHN-290E-95FR containing reconstituted condensates (Fig. 4, F to I). The uniform distribution of PSD-95 in both e/iPSD could be due to the interaction between GPHN-290E-95FR and PSD-95, so that a portion of PSD-95 was sequestered from the ePSD network to iPSD. If this hypothesis is correct, one could reverse PSD-95's partition from iPSD back to ePSD by increasing the ePSD network strength and complexity. To test this, we used Shank3 with the wild-type sterile  $\alpha$ -motif (WT SAM) domain instead of Shank3 with SAM\_ME, which we used as shown in Fig. 4, F and H. Shank3 with SAM\_WT is more potent than the SAM\_ME mutant in forming SAM polymer (40, 50). Indeed, in ePSD condensates with SAM\_WT Shank3, PSD-95 became enriched in the ePSD condensates (Fig. 4, J and K; quantified in fig. S12), supporting the idea that the segregation of ePSD and iPSD is driven by formation of their respective percolated networks.

### iPSD formation rescues mistargeted GPHN-95FR to inhibitory synapses

It is well-established that overexpressed GPHN forms large puncta co-localized with GABA<sub>A</sub>R on dendritic shafts in pyramidal neurons and in interneurons. Because of the segregation of e/iPSD, these GPHN puncta do not overlap with PSD-95 (11, 51) (also see Fig. 5, A and B, left panels). By contrast, overexpressed GPHN-95FR was effectively targeted to dendritic spines in

pyramidal neurons (Fig. 5A, middle panel; also see fig. S14A). In interneurons, GPHN-95FR was also targeted to excitatory synapses marked by PSD-95 (Fig. 5B, middle panel; also see fig. S14B), reminiscent of our in vitro reconstitution results shown in Fig. 4E.

We next asked what might occur if GPHN-95FR was coexpressed with CB in cultured interneurons to enhance iPSD network formation. We found that, in neurons coexpressing CB (CB\_DHPH or FL) and GPHN-95FR, the GPHN-95FR puncta were almost perfectly co-localized with puncta stained with the endogenous GABA<sub>A</sub>R $\gamma$ 2 (Fig. 5C) or GABA<sub>A</sub>R $\alpha$ 1 or  $\alpha$ 2 (fig. S15, A and B). Additionally, with CB coexpression, more GPHN-95FR puncta-containing postsynapses were innervated by inhibitory presynaptic boutons instead of excitatory boutons (figs. S15 and S16), suggesting that phase separation-mediated formation of iPSD condensates by CB, GPHN-95FR, and GABA<sub>A</sub> receptor forced dissociation of GPHN-95FR from ePSD condensates.

The small volume of dendritic spines has made it challenging to investigate phase separation-mediated ePSD formation and segregation of iPSD and ePSD in living neurons because of the resolution limit of conventional optical microscopy. To overcome this challenge, we resorted to single molecule-based direct stochastic optical reconstruction microscopy (dSTORM) super-resolution imaging (15, 52–54), also by taking the advantage that 95FR-tagged GPHN and CB were effectively targeted to dendritic spines in cultured pyramidal neurons (Fig. 5B and fig. S14). When hemagglutinin (HA)-tagged GPHN-95FR alone was overexpressed in pyramidal neurons, the GPHN-95FR signals stained with anti-HA antibody overlapped with the endogenous PSD-95 signals in spine heads (Fig. 5D). We calculated the localization-based overlapping coefficient of the imaged molecules to quantify the degree of co-localization between GPHN-95FR and PSD-95 (Fig. 5E). We used two different antibodies (anti-HA and anti-GPHN) to image GPHN-95FR-HA and regarded the derived overlap coefficient of the two antibody signals as the maximal possible

value obtainable by this method (Fig. 5E, first column). The overlap coefficient of overexpressed GPHN signals to that of endogenous PSD-95 signals on shafts of interneurons is the minimal possible value because two proteins are completely separated (Fig. 5E, last column). We found that the degree of the overlap between GPHN-95FR and PSD-95 in spine heads was almost the same as the degree of the overlap between endogenous Shank and Homer1, which are two well-known co-clustered ePSD proteins (Fig. 5E, second versus fifth column). When GPHN-95FR was coexpressed with 95FR-tagged CB\_DHPH or full-length CB, GPHN-95FR formed nanodomain-like clusters that were separated from PSD-95 clusters in spine heads (Fig. 5D, bottom left row; quantified in Fig. 5E). Because endogenous iPSD proteins are scarcely located in spine heads, we conclude that the segregation of GPHN-95FR from ePSDs was caused by phase separation upon coexpression of CB-95FR. We also verified the segregation of GPHN-95FR in interneurons using super-resolution imaging. Coexpression of GPHN-95FR with CB could effectively dissociate GPHN-95FR from the PSD-95 nanoclusters and induce formation of discrete GPHN-95FR clusters (fig. S17).

We next overexpressed GPHN-95FR-mCherry or GPHN-95FR-mCherry together with CB-95FR-GFP in hippocampi of E14.5 to 15.5 mouse pups by in utero electroporation. We then imaged the localizations of GPHN-95FR-mCherry and CB-95FR-GFP with endogenous inhibitory synapse markers surface GABA<sub>A</sub>R $\gamma$ 2 (*sy*2) and neuroligin2 (NL2) in cultured transfected hippocampal neurons (Fig. 5, F and G). The GPHN-95FR-mCherry/CB-95FR-GFP puncta formed on dendritic spines were also marked by NL2 and GABA<sub>A</sub>R $\gamma$ 2 (Fig. 5, F and G), indicating de novo formation of inhibitory synapses on dendritic spines in vivo.

### Discussion

We show in this study that the iPSD and ePSD condensates are spontaneously segregated from each other even within small subcellular compartments of dendritic spines. Formation

of iPSD and ePSD condensates could generate sufficiently large free energy capable of dissociating a tight binding between PSD-95 and GPHN-95FR. In a broader perspective,

phase separation-mediated membraneless organelle formation can radically change interaction specificities and consequently cellular localizations of biomolecules in living cells.

What might be the molecular mechanism underlying the specific segregation between the ePSD and iPSD condensates? Biological condensates can form percolated molecular

#### Fig. 4. Phase separation forces 95FR-tagged GPHN to dissociate from ePSD condensates and become enriched in iPSD condensates.

(A) Isothermal titration calorimetry (ITC)-based measurement of the binding affinity between 95FR and PSD-95\_PSG. 100  $\mu$ M PSD-95\_PSG was titrated with 10  $\mu$ M PSD-95.FingR.

(B) Schematic diagram showing the designed chimeric proteins composed of GPHN or GPHN 290-736 linked with 95FR by two glycine-glycine-serine (GGS) repeats. (C) (Left) SEC-MALS (size-exclusion chromatography-multiangle light scattering) assay showing that purified GPHN-290E-95FR could form a 1:1 stoichiometric complex with PSD-95\_PSG. 20  $\mu$ M GPHN-290E-95FR, 40  $\mu$ M PSD-95\_PSG, or a mixture of the two proteins at these concentrations were individually assayed. The fitted molecular weights were expressed as the best-fitted values  $\pm$  SD. (Right) SDS-polyacrylamide gel electrophoresis (SDS-PAGE) showing the compositions of proteins in the indicated fractions of the elution profile of the PSD-95\_PSG and GPHN-290E-95FR mixture.

This SDS-PAGE analysis showed that a stable 1:1 PSD-95\_PSG/GPHN-290E-95FR was formed and that the excess amount of PSD-95\_PSG was eluted as a separate peak. (D) Fluorescence images showing mixtures of 4xiPSD condensates with PSD-95 alone. (Left) GPHN-290E was used in the 4xiPSD condensates. (Middle) 95FR-tagged GPHN was used in the 4xiPSD condensates. (Right) Quantification of mean intensities of PSD-95 signals in iPSD droplets. *t* test was applied in the quantification. \*\*\*\**P* < 0.0001. Error bars indicate  $\pm$  SD with *n* = 3 (i.e., three different batches of experiments).

(E) Fluorescence images showing mixtures of 5xePSD with GPHN or 95FR-tagged GPHN. (Left) GPHN-290E was mixed with 5xePSD. (Middle) 95FR-tagged GPHN was mixed with 5xePSD. (Right) Quantification of mean intensities of GPHN signals in ePSD droplets. *t* test was used in the quantification. \*\*\**P* < 0.001. Error bars indicate  $\pm$  SD with *n* = 3 (i.e., three different batches of experiments).

(F to K) Phase separation of iPSD induces

dissociation of 95FR-tagged GPHN from ePSD. In (F) and (H), fluorescence imaging shows that mixing other iPSD scaffold proteins to form 3x or 4xiPSD condensates could induce dissociation of GPHN-290E-95FR from 5xePSD condensates. In (J), fluorescence imaging shows that including Shank3-SAM\_WT in 5xePSD condensates could prevent PSD-95 from entering into 4xiPSD condensates containing GPHN-290E-95FR. (G) shows a line plot analysis of fluorescence signal intensities along the dashed line in (F); (I) shows a line plot analysis of fluorescence signal intensities along the dashed line in (H); and (K) shows a line plot analysis of fluorescence signal intensities along the dashed line in (J). Scale bars, 10  $\mu$ m for all panels. Phosphorylated GKAP was used to enhance the ePSD condensates formation.

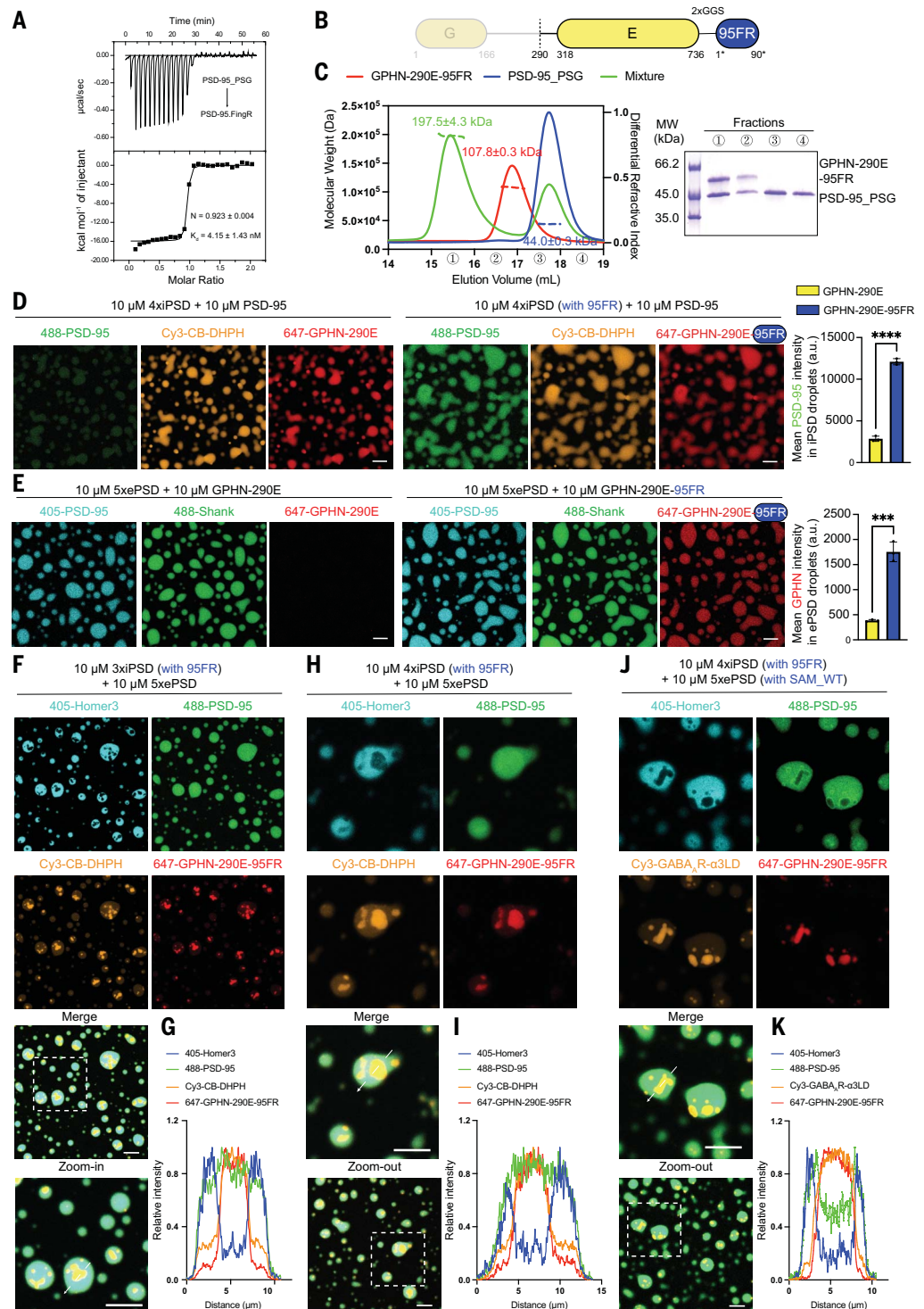


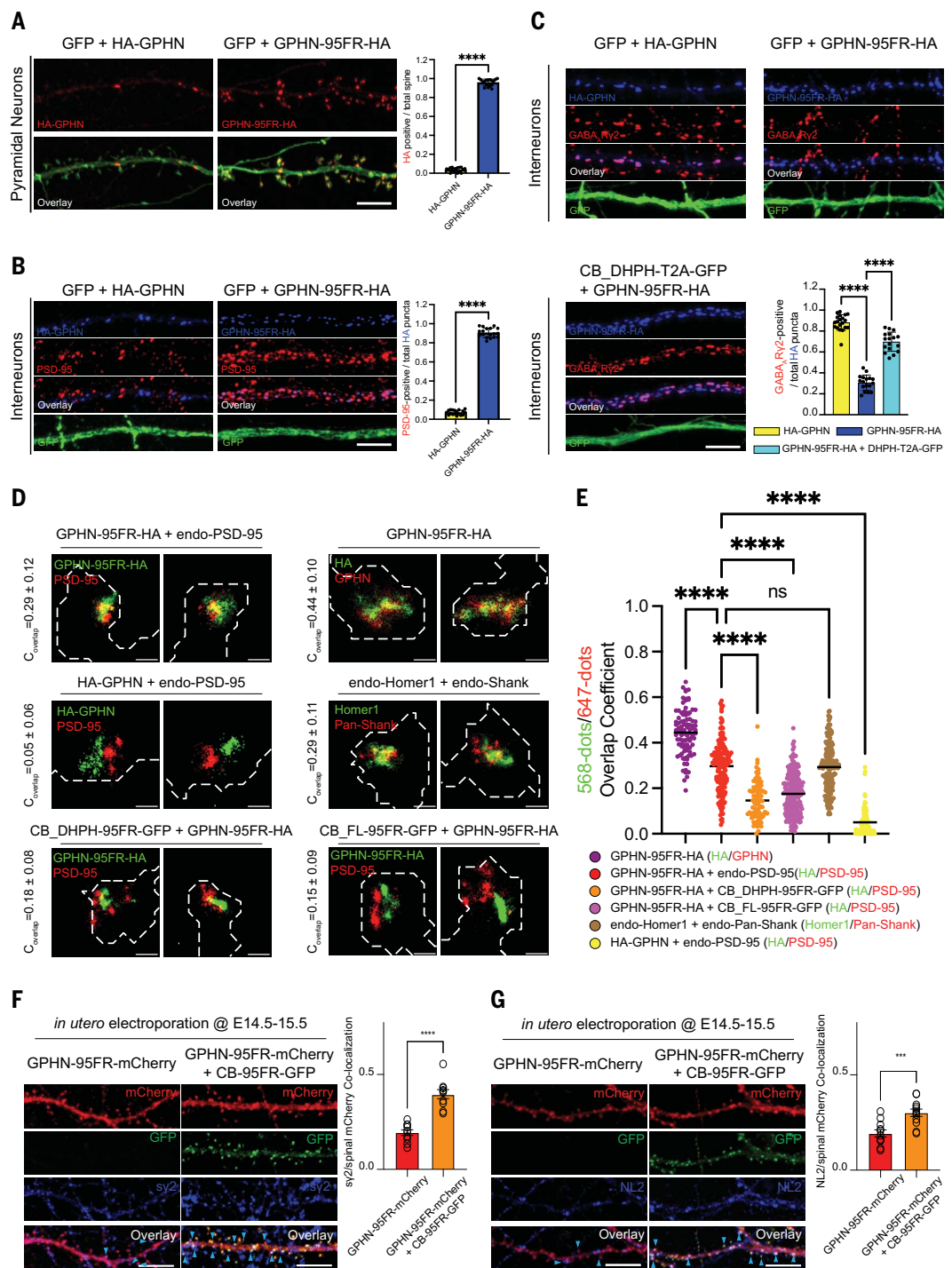
### Fig. 5. Coexpression of CB rescues mistargeted GPHN-95FR to inhibitory synapses in cultured rat hippocampal neurons.

(A and B) Fluorescence images showing the localization of overexpressed GPHN (left) and GPHN-95FR (middle) along dendrites of cultured pyramidal neurons (A) or interneurons (B). (Right) Quantification of the ratio of spines with HA-positive puncta versus total spines (A) or the ratio of HA puncta with PSD-95 signals versus total puncta (B).

$n = 18$  (18 neurons from three different batches of cultures) for each group. (C) Fluorescence images showing the colocalization of overexpressed GPHN or GPHN-95FR with endogenous  $GABA_A\text{R}\gamma 2$  along dendrites of cultured interneurons: (top left) overexpression of GPHN only; (top right) overexpression of GPHN-95FR only; (bottom left) GPHN-95FR coexpressed with CB\_DHPH; and (bottom right) showing the quantification.

HA-GPHN:  $n = 19$ ; GPHN-95FR-HA:  $n = 17$ ; GPHN coexpressed with CB\_DHPH:  $n = 19$ . Data were collected from three different batches of cultures for each group. (D) Representative dSTORM images showing the localization of GPHN-95FR in spine heads in cultured rat pyramidal neurons. (Top row) Only GPHN-95FR was overexpressed. (Left) Imaging of GPHN-95FR and endogenous PSD-95. (Right) Imaging of GPHN-95FR by double staining with an anti-HA antibody and an anti-GPHN antibody. (Middle row, left) Imaging of overexpressed HA-GPHN and endogenous PSD-95 on shafts in interneurons. (Middle row, right) Imaging of endogenous Homer1 and Shank. (Bottom row) GPHN-95FR was coexpressed with the CB DHPH tandem or with the full-length CB. GPHN-95FR and endogenous PSD-95 were imaged. White dashed lines show the outline of postsynapses that were generated with the wide-field images of the GFP channel. Calculated overlap coefficient for each group is marked at the left side of each row and expressed as average  $\pm$  SD.

(E) Scatter plot showing the distribution of calculated overlap coefficients of imaged molecules in each synapse. The datasets (from left to right) were obtained from 94, 151, 80, 232, and 177 spines, and 96 synapses on shafts from six neurons in two different batches of cultures. (F) (Left) Fluorescence images showing the co-localization of overexpressed GPHN-95FR-mCherry only (left column) or with CB-95FR-EGFP (middle column) and endogenous surface  $GABA_A\text{R}\gamma 2$  ( $sy2$ ) in cultured hippocampal neurons from transfected mouse embryos. Blue arrowheads indicate spines with surface  $GABA_A\text{R}\gamma 2$  ( $sy2$ ). (Right) Quantification of the ratio of spinal  $sy2$  puncta versus all spinal mCherry puncta. For GPHN-95FR-mCherry only,  $n = 8$ ; GPHN-95FR-mCherry coexpressed with CB-95FR-EGFP,  $n = 10$ . (G) (Left) Fluorescence images showing the



colocalization of overexpressed GPHN-95FR-mCherry only (left column) or with CB-95FR-EGFP (middle column) and endogenous neuroigin 2 (NL2) in cultured hippocampal neurons from transfected mouse embryos. Blue arrowheads indicate spines with neuroigin 2 (NL2). (Right) Quantification of the ratio of spinal NL2 puncta versus all spinal mCherry puncta. For GPHN-95FR-mCherry only,  $n = 10$ ; GPHN-95FR-mCherry coexpressed with CB-95FR-EGFP,  $n = 11$ . Pyramidal neurons were identified by their pyramidal-shaped soma and dendrites with numerous spine protrusions. Neurons that were stained positive for GAD2/65 and did not contain spines were identified as interneurons. Scale bar, 10  $\mu\text{m}$  for (A) to (C), (F), and (G); 200 nm for (D). Error bars indicate  $\pm$  SD. In (A), (B), (F), and (G),  $t$  test was applied. In (C) and (E), one-way analysis of variance (ANOVA) followed by Tukey's post hoc test was used. \*\*\*\* $P < 0.0001$ . \*\*\* $P < 0.001$ . ns, not significant.

networks (55). We recently demonstrated that both the network complexity and dynamic properties of percolated molecular networks are directly correlated with the affinities and valences of the molecular interactions in a condensate system (40). Molecular condensates formed through specific, strong and high-valent interactions (e.g., the e/iPSD condensates) are highly percolated (see fig. S18 for a model). Molecules trapped in such highly percolated networks have low mobilities (40) (Fig. 3, D to F). One might envision that forced mixing of molecular components from iPSD and ePSD condensates requires breakage of at least one percolated network, a process that is energy costly and thus does not happen easily. Indeed, we demonstrated that the ePSD and iPSD condensates could not be forced to mix even by artificially installing a strong interaction between PSD-95 and GPHN. Therefore, biological condensates formed through specific and multivalent interactions have intrinsic capabilities to form segregated organelle-like structures in cells (fig. S18).

In addition to answering why iPSDs and ePSDs segregate from each other in neurons, our study has uncovered a fundamental principle underlying why different biological condensates formed through phase separation can exist as distinct organelle-like structures in cells. Our study reveals that formation of biological condensates can substantially alter molecular interactions that occur in dilute solutions, a finding that has general implications for understanding functions of biomolecules in cells and for devising strategies in targeting biomolecules or biomolecular networks for translational purposes.

#### REFERENCES AND NOTES

1. C. Q. Chiu *et al.*, *Science* **340**, 759–762 (2013).
2. F. E. Müllner, C. J. Wierenga, T. Bonhoeffer, *Neuron* **87**, 576–589 (2015).
3. C. L. Tao *et al.*, *J. Neurosci.* **38**, 1493–1510 (2018).

4. A. Peters, S. L. Palay, *J. Neurocytol.* **25**, 687–700 (1996).
5. M. Colonnier, *Brain Res.* **9**, 268–287 (1968).
6. Y. T. Liu *et al.*, *Nat. Neurosci.* **23**, 1589–1596 (2020).
7. S. A. Maynard *et al.*, *eLife* **10**, e74441 (2021).
8. D. M. Iacone *et al.*, *Neuron* **106**, 566–578.e8 (2020).
9. O. Gemin *et al.*, *PLoS Biol.* **19**, e3001375 (2021).
10. J. L. Chen *et al.*, *Neuron* **74**, 361–373 (2012).
11. K. L. Villa *et al.*, *Neuron* **89**, 756–769 (2016).
12. M. Fossati *et al.*, *Neuron* **91**, 356–369 (2016).
13. Y. Kubota, S. Hatada, S. Kondo, F. Karube, Y. Kawaguchi, *J. Neurosci.* **27**, 1139–1150 (2007).
14. M. S. Kleinjan *et al.*, *Neuron* **111**, 362–371.e6 (2023).
15. K. C. Crosby *et al.*, *Cell Rep.* **26**, 3284–3297.e3 (2019).
16. A. Uezu *et al.*, *Science* **353**, 1123–1129 (2016).
17. J. Zhu, Y. Shang, M. Zhang, *Nat. Rev. Neurosci.* **17**, 209–223 (2016).
18. M. Sheng, C. C. Hoogenraad, *Annu. Rev. Biochem.* **76**, 823–847 (2007).
19. S. K. Tyagarajan, J. M. Fritschy, *Nat. Rev. Neurosci.* **15**, 141–156 (2014).
20. G. Bai, Y. Wang, M. Zhang, *Cell Res.* **31**, 312–325 (2021).
21. M. Zeng *et al.*, *Neuron* **104**, 529–543.e6 (2019).
22. M. Zeng *et al.*, *Cell* **174**, 1172–1187.e16 (2018).
23. M. Zeng *et al.*, *Cell* **166**, 1163–1175.e12 (2016).
24. M. Feric *et al.*, *Cell* **165**, 1686–1697 (2016).
25. S. Boeynaems *et al.*, *Trends Cell Biol.* **28**, 420–435 (2018).
26. L. Wang *et al.*, *Cell* **185**, 4376–4393.e18 (2022).
27. S. E. Anton *et al.*, *Cell* **185**, 1130–1142.e11 (2022).
28. Q. Su, S. Mehta, J. Zhang, *Mol. Cell* **81**, 4137–4146 (2021).
29. D. L. J. Lafontaine, J. A. Riback, R. Bascetin, C. P. Brangwynne, *Nat. Rev. Mol. Cell Biol.* **22**, 165–182 (2021).
30. B. Dejanovic *et al.*, *EMBO Mol. Med.* **7**, 1580–1594 (2015).
31. C. Sala *et al.*, *J. Neurosci.* **23**, 6327–6337 (2003).
32. G. H. Diering *et al.*, *Science* **355**, 511–515 (2017).
33. V. B. Kasaragod, H. Schindelin, *Front. Mol. Neurosci.* **11**, 317 (2018).
34. T. Soykan *et al.*, *EMBO J.* **33**, 2113–2133 (2014).
35. T. Papadopoulos *et al.*, *EMBO J.* **26**, 3888–3899 (2007).
36. S. Kins, H. Betz, J. Kirsch, *Nat. Neurosci.* **3**, 22–29 (2000).
37. S. Xiang *et al.*, *J. Mol. Biol.* **359**, 35–46 (2006).
38. S. A. Maynard, J. Ranft, A. Triller, *Nat. Rev. Neurosci.* **24**, 4–22 (2023).
39. D. Choquet, A. Triller, *Neuron* **80**, 691–703 (2013).
40. Z. Shen *et al.*, *eLife* **12**, e81907 (2023).
41. C. Charrier, M.-V. Ehrensperger, M. Dahan, S. Lévi, A. Triller, *J. Neurosci.* **26**, 8502–8511 (2006).
42. M. Dahan *et al.*, *Science* **302**, 442–445 (2003).
43. C. Tardin, L. Cognet, C. Bats, B. Lounis, D. Choquet, *EMBO J.* **22**, 4656–4665 (2003).
44. M.-V. Ehrensperger, C. Hanus, C. Vannier, A. Triller, M. Dahan, *Biophys. J.* **92**, 3706–3718 (2007).
45. A. Triller, D. Choquet, *Trends Neurosci.* **28**, 133–139 (2005).
46. C. G. Specht *et al.*, *Neuron* **79**, 308–321 (2013).
47. N. Durisic *et al.*, *J. Neurosci.* **32**, 12915–12920 (2012).
48. G. G. Gross *et al.*, *Neuron* **78**, 971–985 (2013).
49. S. Sensussen *et al.*, *iScience* **23**, 101330 (2020).
50. M. K. Baron *et al.*, *Science* **311**, 531–535 (2006).

51. T.-T. Chiou *et al.*, *J. Biol. Chem.* **286**, 22456–22468 (2011).
52. A. Dani, B. Huang, J. Bergan, C. Dulac, X. Zhuang, *Neuron* **68**, 843–856 (2010).
53. T. Hosokawa *et al.*, *Nat. Neurosci.* **24**, 777–785 (2021).
54. A. H. Tang *et al.*, *Nature* **536**, 210–214 (2016).
55. T. Mittag, R. V. Pappu, *Mol. Cell* **82**, 2201–2214 (2022).
56. J. Zhu *et al.*, *Cell Rep.* **21**, 3781–3793 (2017).
57. H. Wu *et al.*, *Mol. Cell* **84**, 309–326.e7 (2024).

#### ACKNOWLEDGMENTS

We thank members of the Zhang laboratory for comments on the manuscript, Q. Tian from the Lu laboratory for help on in utero electroporation and mouse hippocampal neuronal culture, and the Biosciences Central Research Facility, HKUST, for providing super-resolution imaging microscopy. **Funding:** This research was supported by Ministry of Science and Technology of China grant 2019YFA0508402 (M.Z.), National Natural Science Foundation of China grant 82188101 (M.Z.), Shenzhen Talent Program grant KQTD20210811090115021 (M.Z.), Shenzhen Science and Technology Basic Research Program grant JCYJ20220818100215033 (M.Z.), Guangdong Innovative and Entrepreneurial Research Team Program grant 2021ZT09Y104 (M.Z.), Shenzhen Bay Laboratory grant S201101002 (M.Z.), Research Grant Council of Hong Kong grant 16104518 (M.Z.), Research Grant Council of Hong Kong grant 16101419 (M.Z.), an NIH Intramural Research Program grant (W.L.), and by a postdoctoral fellowship from the Research Grant Council of Hong Kong, HKUST PDFS2122-6S04 (X.W.). **Author contributions:** Conceptualization: S.Z., Z.S., and M.Z. Methodology: S.Z., Z.S., X.W., W.H., and B.J. Investigation: S.Z., Z.S., X.W., W.H., B.J., W.L., and M.Z. Visualization: S.Z., Z.S., and W.H. Funding acquisition: W.L. and M.Z. Project administration: M.Z. Supervision: W.L. and M.Z. Writing – original draft: S.Z., Z.S., and M.Z. Writing – review and editing: S.Z., Z.S., and M.Z. **Competing interests:** The authors declare that they have no competing interests. **Data and materials availability:** All data are available in the main text or the supplementary materials. **License information:** Copyright © 2024 the authors, some rights reserved; exclusive licensee American Association for the Advancement of Science. No claim to original US government works. <https://www.science.org/about/science-licenses-journal-article-reuse>

#### SUPPLEMENTARY MATERIALS

[science.org/doi/10.1126/science.adj7066](https://doi.org/10.1126/science.adj7066)

Materials and Methods

Figs. S1 to S18

Table S1

Movies S1 to S3

References (58–61)

MDAR Reproducibility Checklist

Submitted 11 July 2023; resubmitted 29 December 2023

Accepted 15 April 2024

10.1126/science.adj7066